

# STABILITY OF SUPERSONIC SWEEP-WING BOUNDARY LAYERS WITH OR WITHOUT CROSSFLOW

Toshiyuki Nomura\*

\*Japan Aerospace Exploration Agency

**Keywords:** *Swept Wing, Supersonic Boundary Layer, Streamwise Instability, Crossflow Instability, First-Mode Wave*

## Abstract

*Three-dimensional supersonic boundary layers over an infinite swept wing, which is made from the semispan model of our experimental airplane, are subject to both streamwise and crossflow instabilities. In order to clarify the effects of these instabilities on the spatial growth of first-mode waves, we perform linear stability analysis first with the full boundary layers over the infinite swept wing and next with those without crossflow. It is found that the spatial growth of first-mode waves is mainly due to crossflow instability in the presence of moderate crossflow yielded by favorable pressure gradient. Although a flat pressure distribution at the wing surface restrains crossflow instability, streamwise instability still destabilizes first-mode waves to some extent. Wall cooling will be valid for suppressing streamwise instability.*

## 1 Introduction

Three-dimensional compressible boundary layers over swept wings are subject to both streamwise and crossflow instabilities, which are attributed to boundary-layer profiles in the streamwise and crossflow directions, respectively (see Fig. 1). Furthermore, streamwise instability is divided into viscous and inflectional instabilities. Viscous instability means that the maximum growth rate of a disturbance increases as the Reynolds number decreases. Meanwhile, if there is a generalized inflection point in the streamwise boundary layer, it can cause an inviscid disturbance to grow. In case of swept wings, the disagreement

between the directions of the pressure gradient and the external streamline yields crossflow in the boundary layer. Crossflow is normal to the external streamline and generally directed toward the concave side of the external streamline. Since the crossflow velocity profile always has an inflection point, the boundary layer undergoes inflectional instability called crossflow instability. Crossflow instability amplifies both stationary and traveling disturbances, whereas streamwise instability amplifies traveling ones only.

The stability of three-dimensional supersonic boundary layers was investigated with linear stability theory by Asai, Saitoh, Seino, and Itoh [1] and Balakumar and Reed [2]. Asai et al. dealt with supersonic boundary layers obtained as the extension of the Falkner-Skan-Cooke profiles. Their results indicate that the first-mode wave with the wave angle of about 75° is the most amplified of all the disturbances if the maximum crossflow velocity exceeds about 4% of the external streamwise velocity. First-mode waves in compressible flows correspond to Tollmien-Schlichting waves in incompressible ones. Balakumar and Reed used supersonic boundary layers over a rotating cone at zero angle of attack. Their results show that the growth rate of a first-mode wave is increased by a factor of 2 to 4 due to crossflow in comparison with a two-dimensional flow with the same streamwise profile.

In this study, we examine the stability of three-dimensional supersonic boundary layers over a practical configuration, which is an infinite swept wing made from the semispan model of our experimental airplane. The original wing was designed so as to yield little

crossflow over the upper surface on a cruise [3]. In order to explore each of streamwise and crossflow instabilities, we perform linear stability analysis first with the full boundary-layer profiles and next with the streamwise ones only. The comparison of the results reveals the dominant instability of the swept-wing boundary layers. Accordingly, we find a key for further laminar flow control.

## 2 Numerical Methods

### 2.1 Procedure

Linear stability analysis of three-dimensional compressible boundary layers is conducted using a prediction system of boundary-layer transition [4]. Figure 2 shows the procedure of the prediction system. A compressible flow past a body is computed by the Navier-Stokes (NS) code, and the mean boundary-layer flow is extracted from the converged flow. An initial disturbance in the boundary layer is searched for by the temporal stability code and the spatial stability code, and the spatial growth of the disturbance is computed by the space-marching code. Eventually, the  $N$  factor is obtained by integrating the spatial growth rates of the disturbance.

### 2.2 Navier-Stokes Code

The governing equations of the NS code are the conservation-law form of the thin-layer NS equations. Let  $\xi$ ,  $\eta$ ,  $\zeta$ , and  $\tau$  be the surface coordinate in the normal-chord direction, the wall-normal coordinate, the spanwise coordinate, and time;  $\hat{Q}$  the vector of dependent variables;  $\hat{E}$ ,  $\hat{F}$ , and  $\hat{G}$  the inviscid-flux vectors;  $\hat{F}_v$  the viscous-flux vector; and  $Re$  the Reynolds number. Then, the thin-layer NS equations in generalized curvilinear coordinates can be written as

$$\frac{\partial \hat{Q}}{\partial \tau} + \frac{\partial \hat{E}}{\partial \xi} + \frac{\partial \hat{F}}{\partial \eta} + \frac{\partial \hat{G}}{\partial \zeta} = \frac{1}{Re} \frac{\partial \hat{F}_v}{\partial \eta}, \quad (1)$$

which are numerically solved with a finite-volume method. The inviscid-flux vectors  $\hat{E}$ ,  $\hat{F}$ , and  $\hat{G}$  of third-order accuracy in space and the viscous-flux vector  $\hat{F}_v$  of second-order accuracy in space are computed by the Chakravarthy-Osher TVD scheme [5] and Gauss's theorem, respectively. The diagonalized ADI scheme proposed by Pulliam and Chaussee [6] is used for time integration. The details of the NS code are described in [7].

### 2.3 Stability Analysis Codes

An instantaneous flow may be represented as the sum of a mean flow denoted by  $(\bar{\cdot})$  and a disturbance denoted by  $(\tilde{\cdot})$

$$\begin{aligned} u &= \bar{u} + \tilde{u}, \quad v = \bar{v} + \tilde{v}, \quad w = \bar{w} + \tilde{w}, \\ \rho &= \bar{\rho} + \tilde{\rho}, \quad T = \bar{T} + \tilde{T}, \end{aligned} \quad (2)$$

where  $u$ ,  $v$ ,  $w$  are the velocity components in Cartesian coordinates  $x$ ,  $y$ , and  $z$ , respectively;  $\rho$  the density; and  $T$  the temperature. The mean flow is computed by the NS code. A disturbance in a boundary layer that is nonparallel to the  $\xi$  direction and constant in the  $\zeta$  direction may be written as

$$\tilde{q}(\xi, \eta, \zeta, \tau) = \hat{q}(\xi, \eta) \exp \left[ i \left\{ \int_{\xi_0}^{\xi} \alpha(\bar{\xi}) d\bar{\xi} + \beta \zeta - \omega \tau \right\} \right], \quad (3)$$

where  $\tilde{q}$  is the disturbance vector defined by  $(\tilde{u}, \tilde{v}, \tilde{\rho}, \tilde{T}, \tilde{w})^T$ ;  $\hat{q}$  the corresponding shape function  $(\hat{u}, \hat{v}, \hat{\rho}, \hat{T}, \hat{w})^T$ ; and the subscript 0 denotes the onset of instability. For temporal stability analysis, the real wavenumbers  $\alpha$  and  $\beta$  are given, and the complex frequency  $\omega$  is sought. The imaginary part of  $\omega$  is the temporal growth rate. On the other hand, for spatial stability analysis in the  $\xi$  direction, the real wavenumber  $\beta$  and the real frequency  $\omega$  are given, and the complex wavenumber  $\alpha$  is sought. The imaginary part of  $-\alpha$  is the spatial growth rate in the  $\xi$  direction. Although both  $\alpha$  and  $\beta$

are normally complex in spatial stability analysis,  $\beta$  is constant on infinite swept bodies, and besides the imaginary part of  $\beta$  is regarded as zero except around the attachment line [8].

Substituting Eqs. (2)–(3) into Eq. (1), subtracting the mean-flow terms, and dropping the quadratic terms of the disturbance quantities, we obtain linear PSE

$$D \hat{q} + A \frac{\partial \hat{q}}{\partial \xi} + B \frac{\partial \hat{q}}{\partial \eta} = V \frac{\partial^2 \hat{q}}{\partial \eta^2}, \quad (4)$$

where  $D$ ,  $A$ ,  $B$ , and  $V$  are  $5 \times 5$  coefficient matrices. The boundary conditions for Eq. (4) are

$$\hat{u} = \hat{v} = \hat{w} = \hat{T} = 0 \quad \text{at the wall } (\eta = 0), \quad (5)$$

$$\hat{u}, \hat{v}, \hat{w}, \hat{\rho}, \hat{T} \rightarrow 0 \quad \text{in the free stream } (\eta \rightarrow \infty).$$

In Eq. (4),  $\partial \hat{q} / \partial \xi$  is approximated with a first-order backward difference, and  $\partial \hat{q} / \partial \eta$  and  $\partial^2 \hat{q} / \partial \eta^2$  are approximated with a second-order central difference.

We use the temporal stability code to search for a disturbance that is temporally the most amplified at a location. Assuming that  $\hat{q}$  is a function of the  $\eta$  coordinate only, Eq. (4) reduces to

$$D \hat{q} + B \frac{d\hat{q}}{d\eta} = V \frac{d^2 \hat{q}}{d\eta^2}. \quad (6)$$

The complex frequency  $\omega$  appears linearly in  $D$  as

$$D = D_t - \omega D'_t. \quad (7)$$

Substituting Eq. (7) into Eq. (6) and multiplying both the sides by  $D_t'^{-1}$ , we obtain

$$D_t'^{-1} D_t \hat{q} + D_t'^{-1} B \frac{d\hat{q}}{d\eta} - D_t'^{-1} V \frac{d^2 \hat{q}}{d\eta^2} = \omega \hat{q}. \quad (8)$$

Equation (8) discretized along with the boundary conditions (5) constitutes a  $5 \times 5$ -block tridiagonal system. This tridiagonal system represents an eigenvalue problem that has  $\omega$  and  $\hat{q}$  as the eigenvalue and eigenfunction, respectively. We obtain all the solutions by applying the QR method [9] to the tridiagonal system. This matrix method does not need any

initial guess for  $\omega$ . In respect of the most amplified disturbance, the real wavenumber  $\beta$  and the real part of  $\omega$  are given to the spatial stability code.

Using the spatial stability code, we convert temporal stability into spatial stability and search for an initial disturbance. Because of the thin-layer approximation, the complex wavenumber  $\alpha$  appears linearly in  $D$  as

$$D = D_s - \alpha D'_s.$$

The same procedure as shown above yields the eigenvalue  $\alpha$  and eigenfunction  $\hat{q}$ . We continue spatial stability analysis upstream in the  $\xi$  direction with  $\beta$  and  $\omega$  fixed. When the spatial growth rate of the disturbance becomes the closest to zero, we regard the disturbance as the initial one for space marching.

The space-marching code is based on the Bertolotti-Herbert method [10]. This code makes space marching of the initial disturbance downstream in the  $\xi$  direction with  $\beta$  and  $\omega$  fixed. Equation (4) with  $\partial \hat{q} / \partial \xi$  discretized is written as

$$\left( D_j + \frac{1}{\Delta \xi} A_j \right) \hat{q}_j + B_j \frac{\partial \hat{q}_j}{\partial \eta} - V_j \frac{\partial^2 \hat{q}_j}{\partial \eta^2} = \frac{1}{\Delta \xi} A_j \hat{q}_{j-1}, \quad (9)$$

where  $\Delta \xi$  and the subscript  $j$  are respectively the grid spacing and index in the  $\xi$  direction. We obtain  $\hat{q}_j$  by inverting the left-hand side of Eq. (9) discretized along with the boundary conditions (5). The shape function  $\hat{q}$  is normalized to resolve the ambiguity of the disturbance  $\tilde{q}$  concerning the  $\xi$  coordinate. The normalization condition based on the disturbance energy  $E_d$  is given by

$$\alpha^{\text{new}} = \alpha^{\text{old}} - i \frac{1}{E_d} \int_V \bar{\rho} \left( \hat{u}^\dagger \frac{\partial \hat{u}}{\partial \xi} + \hat{v}^\dagger \frac{\partial \hat{v}}{\partial \xi} + \hat{w}^\dagger \frac{\partial \hat{w}}{\partial \xi} \right) dV, \quad (10)$$

$$E_d = \int_V \bar{\rho} (|\hat{u}|^2 + |\hat{v}|^2 + |\hat{w}|^2) dV,$$

where  $V$  is the cell volume, and the superscript  $\dagger$  denotes complex conjugates. Equation (10) is the Chang-Malik normalization condition [11] modified for the finite-volume method and

transforms the growth of the disturbance energy in the cells aligned in the  $\eta$  direction into the change in  $\alpha$ . The wavenumber  $\alpha_{j-1}$  is used as the initial value of  $\alpha_j$  included in  $D_j$ . Equations (9)–(10) are repeatedly solved until the change in  $\alpha_j$  becomes less than  $10^{-8}$ . Upon convergence, the same procedure is repeated at  $j+1$ .

With regard to infinite swept bodies, the  $N$  factor is defined simply by

$$N = \ln \left( \frac{A}{A_0} \right) = - \int_{\xi_0}^{\xi} \alpha_i(\bar{\xi}) d\bar{\xi},$$

where  $A$  is the amplitude of the disturbance, and the subscript  $i$  denotes an imaginary part. Although the disturbance environment and the receptivity mechanism determine the initial amplitude  $A_0$ , they are not dealt with in this study.

### 3 Results

#### 3.1 Computational Conditions

We examine the stability of three-dimensional supersonic boundary layers over an infinite swept wing, which is made from the semispan model of our experimental airplane. Figure 3 schematically shows the planform of the semispan model and the airfoil of the infinite swept wing. The sweep angle of the infinite swept wing is  $61.2^\circ$ . The free-stream conditions for numerical analyses are set equal to those for the experiments in [12]. The free-stream Mach number  $M_\infty$  is 2.0. The Reynolds number  $Re_{\infty, \text{MAC}}$  based on the free-stream velocity, the free-stream kinematic viscosity, and the mean aerodynamic chord (MAC) is  $4.7 \times 10^6$ , and the Reynolds number  $Re_{\infty, C}$  based on the free-stream velocity, the free-stream kinematic viscosity, and the chord  $C$  of the infinite swept wing is  $1.94 \times 10^6$ . Two angles of attack  $\alpha = 0^\circ$  and  $2.7^\circ$  are taken as in the experiments.

#### 3.2 Boundary-Layer Profiles

Figure 4 shows pressure distributions computed at the upper surface of the infinite swept wing at  $\alpha = 0^\circ$  and  $2.7^\circ$ .  $X$  is the normal-chord distance from the leading edge, and  $C_p$  the pressure coefficient. The pressure distribution at  $\alpha = 0^\circ$  has favorable gradient from the leading edge to  $X/C = 0.174$ , whereas that at  $\alpha = 2.7^\circ$  is almost flat except for the suction peak near the leading edge.

The wing surface is adiabatic and no-slip. Figures 5(a)–5(b) show velocity profiles over the upper surface at  $\alpha = 0^\circ$ .  $Y$  is the wall-normal distance from the surface;  $V_{\text{CF}}$  the crossflow velocity;  $V_{\text{SW}}$  the streamwise velocity; and  $a_\infty$  the speed of sound in the free stream. Although a boundary-layer edge must be determined before the velocity profiles are drawn, it is defined here as the location where the spanwise velocity becomes 99% of its free-stream value. If the crossflow velocity is turned left from the external-streamline direction, its sign is negative. On the other hand, if the crossflow velocity is turned right from the external-streamline direction, its sign is positive. It is found that the  $V_{\text{CF}}$  profile changes with the pressure gradient. The crossflow appears clearly from  $X/C = 0.0501$  to  $X/C = 0.150$  because of the favorable gradient, and it decreases from  $X/C = 0.200$  to  $X/C = 0.344$  because of the slightly adverse gradient. Again, the crossflow increases from  $X/C = 0.395$  to  $X/C = 0.493$  because of the slightly favorable gradient. The favorable pressure gradient also accelerates the external stream through  $X/C = 0.150$ . The  $V_{\text{SW}}$  profiles hardly change downstream of  $X/C = 0.293$ . Figures 6(a)–6(b) show velocity profiles over the upper surface at  $\alpha = 2.7^\circ$ . The region with favorable pressure gradient as at  $\alpha = 0^\circ$  does not exist near the leading edge, which results in the smaller crossflow, the constant external stream, and the thicker boundary layer. The  $V_{\text{CF}}$  profiles at  $X/C = 0.0501, 0.200, 0.244, 0.395,$  and  $0.493$  become S-shape that has two inflection points on the profile.

The crossflow Reynolds number  $Re_{\text{CF}}$  that indicates the intensity of crossflow instability is defined by

$$Re_{CF} = \frac{|V_{CF}|_{\max} \delta_{0.1}}{v_e},$$

where the subscripts  $e$  and  $\max$  denote a boundary-layer edge and a maximum value, respectively, and  $\delta_{0.1}$  is the largest of the  $Y$  coordinates where  $|V_{CF}|/|V_{CF}|_{\max}$  becomes 0.1. Figure 7 shows the  $Re_{CF}$  curves of the boundary layers over the upper surface at  $\alpha = 0^\circ$  and  $2.7^\circ$ . The  $Re_{CF}$  curve at  $\alpha = 0^\circ$  is found to be similar to the  $C_p$  curve in Fig. 4, which means that the intensity of crossflow instability can be controlled by the pressure distribution. Although the crossflow Reynolds number at  $\alpha = 2.7^\circ$  changes complicatedly, it remains small. The flat pressure distribution at  $\alpha = 2.7^\circ$  seems successful in suppressing crossflow instability.

### 3.3 Stability of the Full Boundary Layers

We investigate the stability of the full swept-wing boundary layers to traveling disturbances. Using the temporal stability code, we search for the most amplified disturbance locally by varying its wave angle  $\psi$  and wavelength  $\lambda$ . The wave angle is varied every ten degrees, and the wavelength is varied so that the ratio of the wavelength to the local boundary-layer thickness  $\delta$  becomes integral. When the direction of the dimensional wavenumber vector agrees with that of the external streamline, the wave angle is zero. The sign of the wave angle is positive in the counterclockwise rotation and negative in the clockwise one (see Fig. 8).

With regard to the swept-wing boundary layer at  $\alpha = 0^\circ$ , we obtain six first-mode waves A, B, C, D, E, and F that are the most amplified locally at  $X/C = 0.0501, 0.0781, 0.101, 0.150, 0.200,$  and  $0.244$ , respectively. Table 1 shows their wave angles, ratios of their wavelengths to the local boundary layer thickness, and frequencies. It is found that the first-mode waves with  $\psi = -70^\circ$  and  $\lambda/\delta = 6$  are the most amplified except at  $X/C = 0.200$ . It is noted from Fig. 5(a) that the maximum absolute value of the crossflow velocity always appears on the side of  $\psi = 90^\circ$ . The spatial growth of the six

first-mode waves is computed from the onset of instability to  $X/C = 0.493$  by the space-marching code, with their spanwise wavenumbers and frequencies fixed. Figure 9 shows the  $N$  factors of the six first-mode waves.

The same procedure as shown above is repeated concerning the swept-wing boundary layer at  $\alpha = 2.7^\circ$ . We obtain six first-mode waves A', B', C', D', E', and F' that are the most amplified locally at  $X/C = 0.0501, 0.0781, 0.101, 0.150, 0.200,$  and  $0.244$ , respectively (see Table 2). As compared with Table 1, the wavelengths in Table 2 are long. It is noted from Fig. 6(a) that the maximum absolute value of the crossflow velocity appears on the side of  $\psi = -90^\circ$  at  $X/C = 0.0501$  and  $0.244$  and on the side of  $\psi = 90^\circ$  at  $X/C = 0.101, 0.150,$  and  $0.200$ . Namely, the wavenumber vectors of the most amplified first-mode waves are directed opposite to the maximum crossflows at all the locations. Figure 10 shows the  $N$  factors of the six first-mode waves. These waves are less amplified than the six first-mode waves at  $\alpha = 0^\circ$ . Although first-mode waves in two-dimensional boundary layers are usually more amplified for zero pressure gradient than for favorable one [13], the results obtained here show the opposite. The three-dimensionality, namely crossflow, of the swept-wing boundary layers is found to have a great effect on the spatial growth of first-mode waves.

### 3.4 Stability of the Boundary Layers without Crossflow

In order to clarify the effect of each instability on the spatial growth of first-mode waves, we investigate the stability of the swept-wing boundary layers where the crossflow velocity is reduced to zero. This means  $V_{CF} \rightarrow 0$  in Figs. 5–6 and besides  $Re_{CF} \rightarrow 0$  in Fig. 7.

In respect of the swept-wing boundary layer without crossflow at  $\alpha = 0^\circ$ , we compute the spatial growth of six first-mode waves that have the same spanwise wavenumbers and frequencies as the six first-mode waves of the last section. The first-mode waves a, b, c, d, e,

and f correspond to the first-mode waves A, B, C, D, E, and F. Figure 11 shows the  $N$  factors of the first-mode waves d–f. The first-mode waves a–c do not grow. The spatial growth of the first-mode waves is found to be crucially restrained by removing the crossflow. It is noticed that the spatial growth shown in Fig. 9 is mainly due to crossflow instability. However, it is noted that the  $\xi$ -direction wavenumbers of the first-mode waves a–f differ slightly from those of their correspondents because of no crossflow. For example, at  $X/C = 0.0501$ , the real part of  $\alpha$  of the first-mode wave a is 1.1 times as large as that of the first-mode wave A. Since the real and imaginary parts of  $\alpha$  are computed simultaneously, it is impossible that its real part only is given.

We repeat the same computations as shown above concerning the swept-wing boundary layer without crossflow at  $\alpha = 2.7^\circ$ . The first-mode waves a', b', c', d', e', and f' correspond to the first-mode waves A', B', C', D', E', and F'. Figure 12 shows the  $N$  factors of the first-mode waves a'–f'. As compared with Fig. 10, the difference is only the slightly gentle gradients of the  $N$ -factor curves. Accordingly, it is found that the spatial growth shown in Fig. 10 is mainly due to streamwise instability. The  $\xi$ -direction wavenumbers of the first-mode waves a'–f' are nearly equal to those of their correspondents.

At  $\alpha = 2.7^\circ$ , the flat pressure distribution at the upper surface of the infinite swept wing prevents first-mode waves from growing owing to crossflow instability. Even without crossflow, however, streamwise instability still destabilizes first-mode waves to some extent. The upper surface of the infinite swept wing with the flat pressure distribution is considered identical with a flat plate. Because wall cooling is valid for suppressing streamwise instability of a flat-plate boundary layer [8], it will also be available for the infinite swept wing.

## 4 Conclusions

In order to clarify the effects of streamwise and crossflow instabilities on the spatial growth of first-mode waves, we have performed linear stability analysis first with the full supersonic boundary layers over an infinite swept wing and next with those without crossflow. It is found that the spatial growth of first-mode waves is mainly due to crossflow instability at the angle of attack of  $0^\circ$ , where the favorable pressure gradient near the leading edge yields moderate crossflow. Although the flat pressure distribution at the wing surface at the angle of attack of  $2.7^\circ$  restrains crossflow instability, streamwise instability still destabilizes first-mode waves to some extent. Wall cooling that is valid for suppressing streamwise instability of a flat-plate boundary layer will also be available for the infinite swept wing.

## References

- [1] Asai, M., Saitoh, N., Seino, H., and Itoh, N. Influence of compressibility on three-dimensional boundary layer stability. *Trans. Japan Soc. Aero. Space Sci.*, Vol. 42, No. 136, pp. 76–84, 1999.
- [2] Balakumar, P. and Reed, H. L. Stability of three-dimensional supersonic boundary layers. *Phys. Fluids A*, Vol. 3, No. 4, pp. 617–632, 1991.
- [3] Ogoshi, H. Aerodynamic design of a supersonic aircraft wing — application of the natural laminar flow concept to airfoil. *Proc. 47th Japan NCTAM*, pp. 341–342, 1998 (in Japanese).
- [4] Nomura, T. Stability analysis of supersonic swept-wing boundary layers. AIAA Paper 2003-4145, 2003.
- [5] Chakravarthy, S. R. Development of upwind schemes for the Euler equations. NASA CR-4043, 1987.
- [6] Pulliam, T. H. and Chaussee, D. S. A diagonal form of an implicit approximate-factorization algorithm. *J. Comput. Phys.*, Vol. 39, pp. 347–363, 1981.
- [7] Nomura, T. Navier-Stokes simulation and linear stability analysis for a boundary layer on the swept cylinder. NAL TR-1321, 1997 (in Japanese).
- [8] Mack, L. M. Boundary-layer linear stability theory. AGARD Report 709, pp. 3/1–81, 1984.
- [9] Wilkinson, J. H. *The algebraic eigenvalue problem*. Clarendon Press, 1965.
- [10] Bertolotti, F. P., Herbert, Th., and Spalart, P. R. Linear and nonlinear stability of the Blasius boundary layer. *J. Fluid Mech.*, Vol. 242, pp. 441–474, 1992.
- [11] Chang, C.-L. and Malik, M. R. Oblique-mode breakdown and secondary instability in supersonic

boundary layers, *J. Fluid Mech.*, Vol. 273, pp. 323–360, 1994.

- [12] Sugiura, H., Noguchi, M., Takagi, S., Tokugawa, N., and Nishizawa, A. Transition characteristics of the non-powered experimental airplane for supersonic transport at Mach 2.0 and 1.2. *Proc. 31st JSASS Annual Meeting*, pp. 170–173, 2000 (in Japanese).
- [13] Masad, J. A. and Zurigat, Y. H. Effect of pressure gradient on first mode of instability in high-speed boundary layers. NASA CR-194910, 1994.

Table 1. Wave Angles, Wavelengths, and Frequencies of the Most Amplified Disturbances at  $\alpha = 0^\circ$ .

Wave	$X/C$	$\Psi$	$\lambda/\delta$	$f^*$ (kHz)
A	0.0501	$-70^\circ$	6	71.8
B	0.0781	$-70^\circ$	6	55.5
C	0.101	$-70^\circ$	6	49.3
D	0.150	$-70^\circ$	6	43.0
E	0.200	$-70^\circ$	5	47.0
F	0.244	$-70^\circ$	6	33.5

Table 2. Wave Angles, Wavelengths, and Frequencies of the Most Amplified Disturbances at  $\alpha = 2.7^\circ$ .

Wave	$X/C$	$\Psi$	$\lambda/\delta$	$f^*$ (kHz)
A'	0.0501	$60^\circ$	7	82.4
B'	0.0781	$60^\circ$	8	59.5
C'	0.101	$-60^\circ$	9	46.0
D'	0.150	$-70^\circ$	7	35.0
E'	0.200	$-70^\circ$	7	29.5
F'	0.244	$70^\circ$	7	24.6

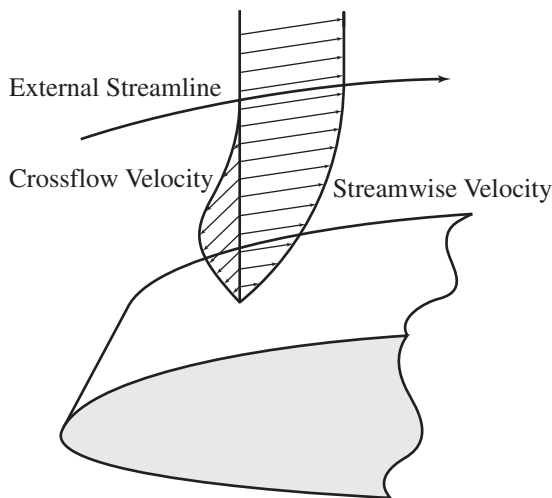


Fig. 1. Boundary-Layer Profiles over a Swept Wing.

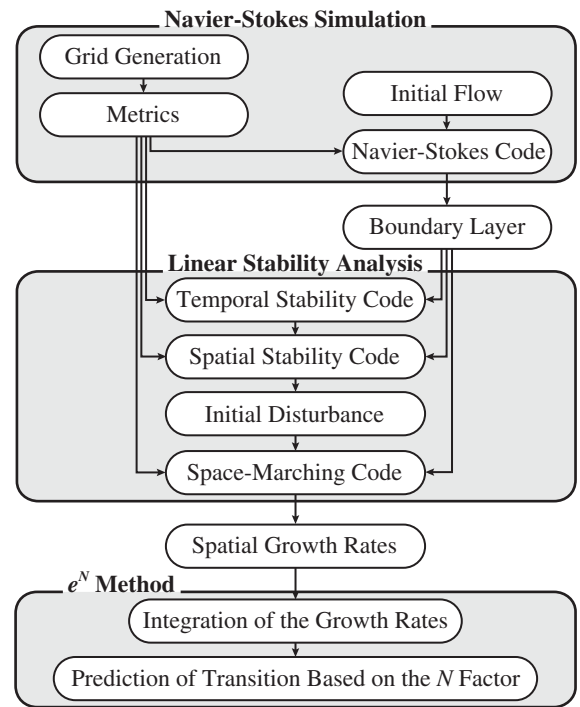


Fig. 2. Procedure for Prediction of Boundary-Layer Transition.

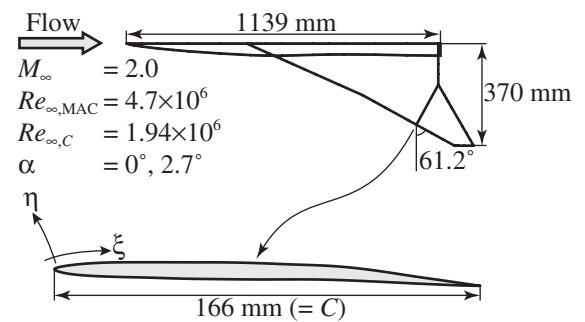


Fig. 3. Schematic of the Semispan Model.

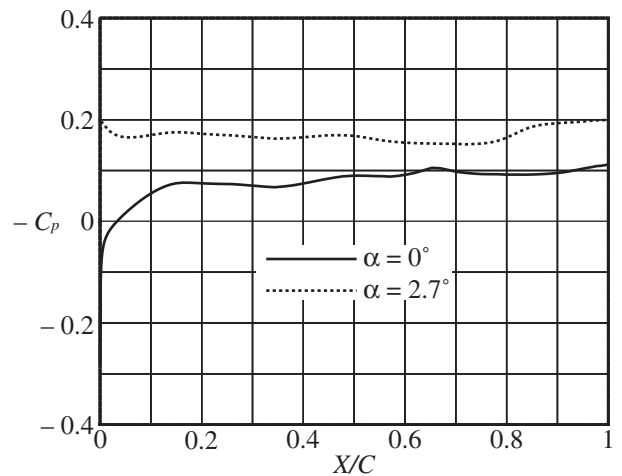


Fig. 4. Pressure Distributions at the Upper Surface of the Infinite Swept Wing.

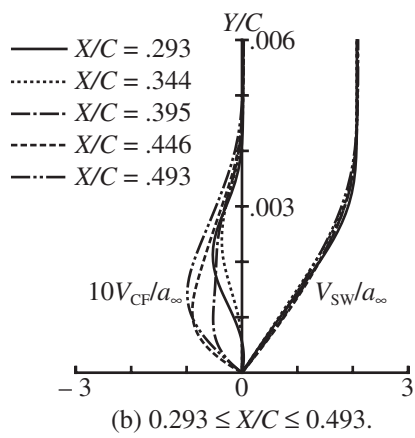
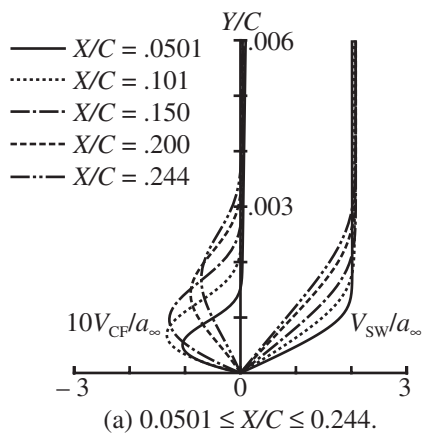


Fig. 5. Velocity Profiles over the Infinite Swept Wing at  $\alpha = 0^\circ$ .

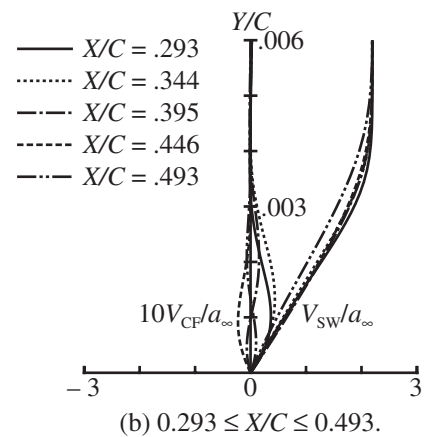
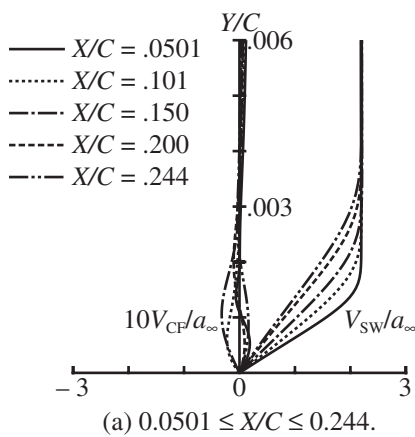


Fig. 6. Velocity Profiles over the Infinite Swept Wing at  $\alpha = 2.7^\circ$ .

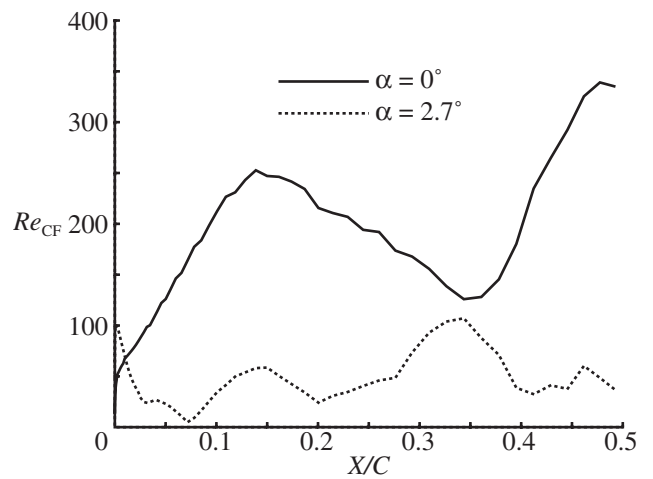


Fig. 7. Crossflow Reynolds Numbers of the Boundary Layers over the Infinite Swept Wing.

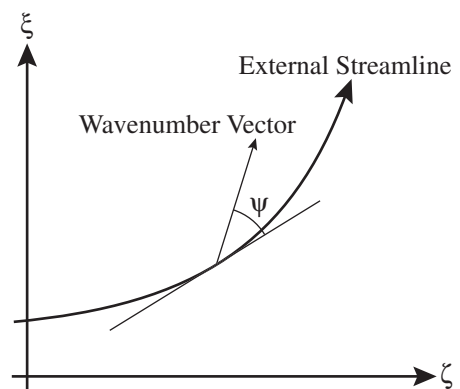


Fig. 8. Wave Angle between a Wavenumber Vector and an External Streamline.

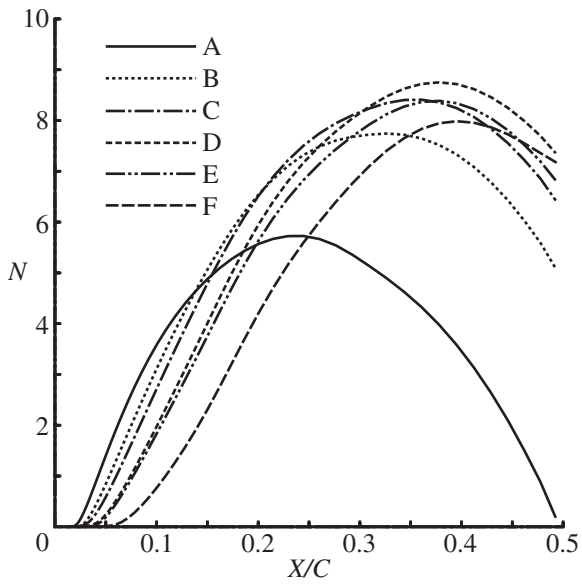


Fig. 9.  $N$  factors with Crossflow at  $\alpha = 0^\circ$ .

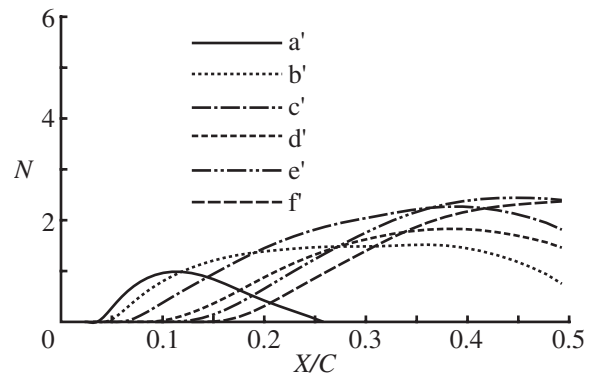


Fig. 12.  $N$  factors without Crossflow at  $\alpha = 2.7^\circ$ .

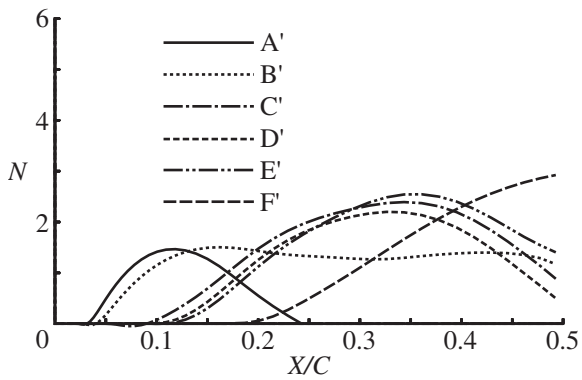


Fig. 10.  $N$  factors with Crossflow at  $\alpha = 2.7^\circ$ .

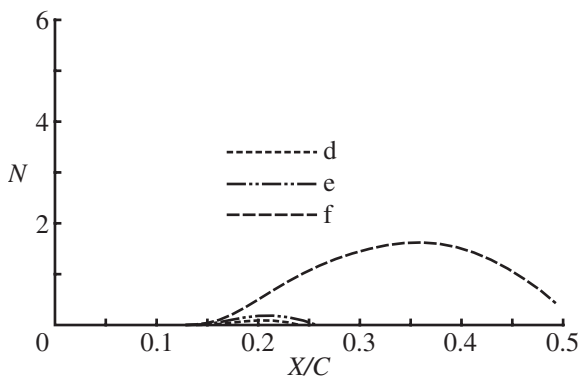


Fig. 11.  $N$  factors without Crossflow at  $\alpha = 0^\circ$ .